Ultrahigh differential mobility and velocity of Néel domain walls in spin valves with planar-transverse polarizers and perpendicularly injected small currents

Mei Li,[1] Zhong An,[2] and Jie Lu[2,*]

[1]*Physics Department, Shijiazhuang University, Shijiazhuang, Hebei 050035, China*

[2]*College of Physics and Information Engineering, Hebei Advanced Thin Films Laboratory, Hebei Normal University, Shijiazhuang 050024, China*

(Received 28 January 2019; revised manuscript received 11 July 2019; published 13 August 2019)

Transverse domain wall (TDW) dynamics in long and narrow spin valves with perpendicular current injection is theoretically investigated. We demonstrate that stable traveling-wave motion of TDWs with finite velocity survives for strong enough planar-transverse polarizers. For typical ferromagnetic materials (for example, Co) and achievable spin polarization ($P = 0.6$), TDWs acquire a velocity of 10^3 m/s under a current density below 10^7 A/cm^2. This efficiency is comparable with that of perpendicular polarizers. More importantly, in this case the wall has ultrahigh "differential mobility" around the onset of stable wall excitations. Our results open possibilities for developing magnetic nanodevices based on TDW propagation with low energy consumption. Also, analytics for parallel and perpendicular polarizers perfectly explains existing simulation findings. Finally, further boosting of TDWs by external uniform transverse magnetic fields is investigated and turns out to be efficient.

DOI: 10.1103/PhysRevB.100.064406

I. INTRODUCTION

Tremendous progress in fabrication technology of nonvolatile magnetic nanodevices has led to a great revolution in modern information industry [1–3]. In these nanodevices, magnetic domains with different orientations build zeros and ones in binary world. Intermediate regions separating these domains are the domain walls (DWs) and their motion leads to the data transformation [4–9]. Generally, DW motion can be induced by magnetic fields, spin-polarized currents, or temperature gradients, etc. Among them, the current-induced case is the easiest to implement in real experiments.

Historically, the earliest current-induced driving mechanism of DWs is the spin-transfer torque (STT). It was first calculated in a magnetic multilayer, in which two ferromagnetic (FM) layers are single domained with "current perpendicular to the plane (CPP)" configuration [10]. The resultant STT is the so-called Slonczewski torque (SLT) and proportional to $\mathbf{m} \times (\mathbf{m} \times \mathbf{m}_p)$ in which $\mathbf{m}$ and $\mathbf{m}_p$ are normalized magnetization vectors in the thin (free) and thick (pinned) layers. Meanwhile, another torque ($\propto \mathbf{m} \times \mathbf{m}_p$) also exists and is usually referred to as the fieldlike torque (FLT) since now $\mathbf{m}_p$ acts like an effective field. Later, in magnetic nanostrips with currents flowing in strip plane (CIP), adiabatic and nonadiabatic STTs are proposed and can be viewed as the continuous limits of SLT and FLT, respectively [11,12]. The adiabatic STT induces the initial DW movement but the final steady wall velocity is determined by the nonadiabatic STT. However, since the exchange interaction avoids abrupt variation of magnetization, CIP current densities of several 10^8 A/cm^2 only induce DW velocity around 100 m/s.

To increase current efficiency, long and narrow spin valves (LNSVs) or magnetic tunneling junctions (MTJs) with CPP configuration are proposed to be host systems [13–15]. In these multilayers, DWs in free layers are driven to move along the long axis by spin-polarized current filtered by pinned layers (polarizers). Early simulations on parallel and perpendicular polarizers only considered SLTs and asserted that the current efficiency can not be increased too much [16,17]. In 2009, a significant breakthrough [18] was made by Khvalkovskiy *et al.* in which numerical simulations with both SLT and FLT revealed that to achieve a DW velocity of 100 m/s, the CPP current density for parallel polarizers is lowered to 10^7 A/cm^2, while for perpendicular polarizers, the CPP current density is further decreased to 10^6 A/cm^2.

Later, two series of experimental works were carried out. First, in LNSVs [19] and half-ring MTJs [20–22] with CPP configuration, transport measurements confirm that DWs can propagate with velocities as high as 500–800 m/s at current density below 10^7 A/cm^2. Second, in zigzag LNSVs with CIP configuration high DW velocities (150–600 m/s) are obtained for current densities of $(2 \sim 5) \times 10^7$ A/cm^2 by using photoemission electron microscopy combined with x-ray magnetic circular dichroism [23–26]. Vertical spin current coming with spin flux transformation from pinned layers to free layers via spacers (thus similar to CPP) is suggested to provide a potential explanation for this velocity boosting.

Except for these concentrated explorations on parallel and perpendicular polarizers, LNSVs with planar-transverse polarizers have not received enough attention in existing literatures. Within a mature Lagrangian framework [27], in this paper we show that stable traveling-wave motion of DWs with finite velocity exists for strong enough planar-transverse polarizers. The resulting current efficiency is comparable with that of perpendicular polarizers. Furthermore, ultrahigh

*jlu@hebtu.edu.cn

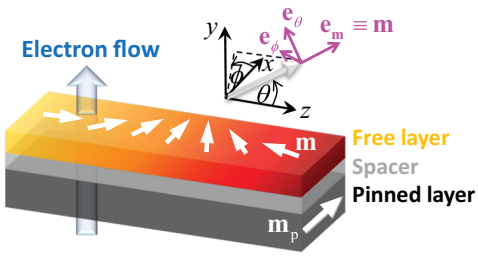

FIG. 1. Sketch of a LNSV with CPP configuration, which is a three-layer structure: a pinned FM layer ($\mathbf{m}_p$, polarizer), a NM metallic spacer and a free FM layer ($\mathbf{m}$). A DW in the free layer is driven to move along the long axis of LNSV by perpendicularly injected currents. ($\mathbf{e}_x$, $\mathbf{e}_y$, $\mathbf{e}_z$) is the global Cartesian coordinate system, and ($\mathbf{e}_\mathbf{m}$, $\mathbf{e}_\theta$, $\mathbf{e}_\phi$) forms the local spherical coordinate system associated with $\mathbf{m}$.

"differential mobility" emerges around the onset of stable wall excitation. Also, we provide analytics for parallel and perpendicular polarizers, which perfectly explains existing simulations. Finally, further boosting of DWs by uniform transverse magnetic fields (UTMFs) are studied with the help of one-dimensional asymptotic expansion method (1D-AEM) [28–32].

II. MODEL AND METHOD

We consider a LNSV with CPP configuration (see Fig. 1), which is composed of three layers: a free FM layer with tunable magnetization texture, a nonmagnetic (NM) metallic spacer, and a pinned FM layer with a fixed magnetization orientation (polarizer). The global Cartesian coordinate system is as follows: $\mathbf{e}_z$ is along the long axis of LNSV, $\mathbf{e}_y$ follows the electron flow direction (from pinned to free layer), and $\mathbf{e}_x = \mathbf{e}_y \times \mathbf{e}_z$. The polarizer is usually made of hard FM materials. Its magnetization ($\mathbf{m}_p$) has three typical choices: (a) $\mathbf{m}_p = \mathbf{e}_z$ (parallel), (b) $\mathbf{m}_p = \mathbf{e}_y$ (perpendicular), and (c) $\mathbf{m}_p = \mathbf{e}_x$ (planar-transverse). Electrons flow from the polarizer to the free layer via the metallic spacer with density $J_e(>0)$. Thus the charge current is $J_{\text{charge}} = -J_e\mathbf{e}_y$.

The normalized magnetization $\mathbf{m}$ of the free layer can be fully described by its polar angle θ and azimuthal angle ϕ. The associated local spherical coordinate system is denoted as ($\mathbf{e}_\mathbf{m}$, $\mathbf{e}_\theta$, $\mathbf{e}_\phi$). Then $\mathbf{m}_p$ is decomposed into

$$\mathbf{m}_p = p_\mathbf{m}\mathbf{e}_\mathbf{m} + p_\theta\mathbf{e}_\theta + p_\phi\mathbf{e}_\phi, \tag{1}$$

with

$$\begin{aligned} p_\mathbf{m} &= \sin\theta_p\cos(\phi-\phi_p)\sin\theta + \cos\theta_p\cos\theta, \\ p_\theta &= \sin\theta_p\cos(\phi-\phi_p)\cos\theta - \cos\theta_p\sin\theta, \\ p_\phi &= -\sin\theta_p\sin(\phi-\phi_p), \end{aligned} \tag{2}$$

where θ_p (ϕ_p) is the polar (azimuthal) angle of $\mathbf{m}_p$.

The magnetic energy of the free layer includes the exchange, crystalline anisotropy, magnetostatic, and FLT-induced effective potential. Following He's work [27], we have

$$\mathscr{E}[\mathbf{m}] = \mathscr{E}_0[\mathbf{m}] - \mu_0 M_s^2 \xi_{\text{CPP}} \frac{J_e}{J_p}\frac{b_p}{c_p}\ln(1+c_p p_\mathbf{m}), \tag{3}$$

with

$$\mathscr{E}_0[\mathbf{m}] = J\left(\frac{\partial\mathbf{m}}{\partial z}\right)^2 + \mu_0 M_s^2\left(-\frac{1}{2}k_E m_z^2 + \frac{1}{2}k_H m_y^2\right), \tag{4}$$

in which the magnetostatic energy has been described by local quadratic terms of $M_{x,y,z}$ by means of three average demagnetization factors [30]. J is the exchange stiffness, μ_0 is the vacuum permeability, ξ_{CPP} describes the relative strength of FLT over SLT, $k_E(k_H)$ is the total anisotropy coefficient along the easy (hard) axis of the free layer, and M_s is the saturation magnetization. In addition, $J_p \equiv 2\mu_0 e d M_s^2/\hbar$ where d is the thickness of free layer, $e(>0)$ is the absolute charge of electron and P is the spin polarization of the current. Finally, the two dimensionless parameters $b_p = 4P^{3/2}/[3(1+P)^3 - 16P^{3/2}]$ and $c_p = (1+P)^3/[3(1+P)^3 - 16P^{3/2}]$ reproduce Slonczewski's original spin polarization factor $g \equiv [-4 + (1+P)^3(3+\mathbf{m}\cdot\mathbf{m}_p)/(4P^{3/2})]^{-1}$ [10] by $g = b_p/(1 + c_p p_\mathbf{m})$.

The magnetization dynamics in the free layer is described by the Lagrangian $L = \int \mathscr{L}\mathrm{d}^3\mathbf{r}$ with density

$$\mathscr{L} = \frac{\mu_0 M_s}{\gamma_0}\dot{\phi}(1-\cos\theta) - \mathscr{E}, \tag{5}$$

in which $\gamma_0 = \mu_0\gamma$ with γ being the gyromagnetic ratio and a dot means $\partial/\partial t$. To include the Gilbert damping and the SLT-induced antidamping processes, an extra dissipation functional $F = \int \mathscr{F}\mathrm{d}^3\mathbf{r}$ is introduced with density

$$\frac{\mathscr{F}}{\mu_0 M_s^2} = \frac{\alpha}{2}\frac{\dot{\theta}^2 + \dot{\phi}^2\sin^2\theta}{\gamma_0 M_s} - g\frac{J_e}{J_p}(p_\theta\sin\theta\dot{\phi} - p_\phi\dot{\theta}). \tag{6}$$

The corresponding generalized Eular-Lagrangian equation

$$\frac{d}{dt}\left(\frac{\delta\mathscr{L}}{\delta\dot{X}}\right) - \frac{\delta\mathscr{L}}{\delta X} + \frac{\delta\mathscr{F}}{\delta\dot{X}} = 0, \tag{7}$$

provides dynamical descriptions of TDWs, where X represents related collective coordinates.

Early simulations confirmed that in FM nanostrips with small enough cross section, transverse DWs (TDWs) have the lowest energy among all metastable states [33,34]. In 2012, further simulations revealed that the stability range of TDW in free layers of LNSVs can be shifted toward larger cross sections compared with monolayer strips, due to a magnetostatic screening effect between the free and pinned layers [35]. Therefore, the configuration space of DWs in this paper is the TDW with generalized Walker profile [36],

$$\ln\tan\frac{\vartheta(z,t)}{2} = \eta\frac{z-q(t)}{\Delta(t)}, \quad \phi(z,t) \equiv \varphi(t), \tag{8}$$

in which $\eta = +1$ or -1 represents head-to-head (HH) or tail-to-tail TDWs, respectively. Note that in many 1D collective-coordinate analysis, the tilting angle $\varphi(t)$ and wall center position $q(t)$ [or wall velocity $\dot{q}(t)$] are the two collective coordinates, meanwhile assuming fixed wall width $\Delta(t)$ [37,38]. However, the wall width does change considerably as the wall tilting angle varies if the material is magnetically biaxial. Even for uniaxial materials, the strip geometry will induce an effective hard axis in the normal direction perpendicular to strip plane. Based on these facts, we therefore view the wall width as the third collective coordinate.

In Eq. (7), by letting X take $q(t)$, $\varphi(t)$, $\Delta(t)$, successively, and integrating over the long axis (i.e., $\int_{-\infty}^{+\infty} dz$), we obtain the following dynamic equations:

$$\frac{\dot{\varphi}+\alpha\eta\dot{q}/\Delta}{\gamma_0 M_s} = b_\mathrm{p}\frac{J_e}{J_\mathrm{p}}\left[p_\varphi U(\varphi) - \frac{\xi_\mathrm{CPP}}{2c_\mathrm{p}}\ln\frac{1-c_\mathrm{p}\cos\theta_\mathrm{p}}{1+c_\mathrm{p}\cos\theta_\mathrm{p}}\right], \tag{9a}$$

$$\frac{\alpha\dot{\varphi}-\eta\dot{q}/\Delta}{\gamma_0 M_s} = b_\mathrm{p}\frac{J_e}{J_\mathrm{p}}\left[\xi_\mathrm{CPP}p_\varphi U(\varphi) + \frac{1}{2c_\mathrm{p}}\ln\frac{1-c_\mathrm{p}\cos\theta_\mathrm{p}}{1+c_\mathrm{p}\cos\theta_\mathrm{p}}\right] - k_\mathrm{H}\sin\varphi\cos\varphi, \tag{9b}$$

$$\frac{\pi^2\alpha}{6\gamma_0 M_s}\frac{\dot{\Delta}}{\Delta} = b_\mathrm{p}\frac{J_e}{J_\mathrm{p}}\left[\xi_\mathrm{CPP}W(\varphi) - p_\varphi U(\varphi)\ln\frac{1-c_\mathrm{p}\cos\theta_\mathrm{p}}{1+c_\mathrm{p}\cos\theta_\mathrm{p}}\right] + \left(\frac{l_0^2}{\Delta^2} - k_\mathrm{E} - k_\mathrm{H}\sin^2\varphi\right), \tag{9c}$$

with

$$\begin{aligned} U(\varphi) &\equiv \chi/\sqrt{1-c_\mathrm{p}^2[\sin^2\theta_\mathrm{p}\cos^2(\varphi-\phi_\mathrm{p})+\cos^2\theta_\mathrm{p}]},\\ W(\varphi) &\equiv \frac{1}{2c_\mathrm{p}}\left[\frac{\pi^2}{4}+\frac{1}{4}\ln^2\frac{1-c_\mathrm{p}\cos\theta_\mathrm{p}}{1+c_\mathrm{p}\cos\theta_\mathrm{p}} - \chi^2\right],\\ \chi &\equiv \arccos\frac{c_\mathrm{p}\sin\theta_\mathrm{p}\cos(\varphi-\phi_\mathrm{p})}{\sqrt{1-c_\mathrm{p}^2\cos^2\theta_\mathrm{p}}}, \end{aligned} \tag{10}$$

and $l_0 \equiv \sqrt{2J/(\mu_0 M_s^2)}$ being the exchange length of the free layer. Note that in the definition of function $W(\varphi)$ in Eqs. (10), our calculation supports an additional "1/2" factor compared with He's original work.

III. DW DYNAMICS UNDER PLANAR-TRANSVERSE POLARIZERS

For planar-transverse polarizers, $\theta_\mathrm{p}=\pi/2$ and $\phi_\mathrm{p}=0$. The dynamical equations evolve to

$$\frac{1+\alpha^2}{\gamma_0 M_s\sin\varphi}\frac{\eta\dot{q}}{\Delta} = \left[k_\mathrm{H}\cos\varphi - (\alpha-\xi_\mathrm{CPP})b_\mathrm{p}\frac{J_e}{J_\mathrm{p}}\widetilde{U}(\varphi)\right], \tag{11a}$$

$$\frac{1+\alpha^2}{\gamma_0 M_s\sin\varphi}\dot{\varphi} = -\left[(1+\alpha\xi_\mathrm{CPP})b_\mathrm{p}\frac{J_e}{J_\mathrm{p}}\widetilde{U}(\varphi) + \alpha k_\mathrm{H}\cos\varphi\right], \tag{11b}$$

$$\frac{\pi^2\alpha}{6\gamma_0 M_s}\frac{\dot{\Delta}}{\Delta} = \left(\frac{l_0^2}{\Delta^2} - k_\mathrm{E} - k_\mathrm{H}\sin^2\varphi\right) + \xi_\mathrm{CPP}b_\mathrm{p}\frac{J_e}{J_\mathrm{p}}\widetilde{W}(\varphi), \tag{11c}$$

in which

$$\begin{aligned} \widetilde{U}(\varphi) &= \frac{\tilde{\chi}}{\sqrt{1-c_\mathrm{p}^2\cos^2\varphi}}, \quad \widetilde{W}(\varphi) = \frac{1}{2c_\mathrm{p}}\left(\frac{\pi^2}{4}-\tilde{\chi}^2\right),\\ \tilde{\chi} &= \arccos(c_\mathrm{p}\cos\varphi). \end{aligned} \tag{12}$$

For steady traveling-wave mode, $\dot{\varphi}=0$ and $\dot{\Delta}=0$. This leads to two branches of solution:

$$\begin{aligned} &\varphi_0 = n\pi, \quad v_0 = 0,\\ &\Delta(\varphi_0) = l_0\left[k_\mathrm{E} - \xi_\mathrm{CPP}b_\mathrm{p}\frac{J_e}{J_\mathrm{p}}\widetilde{W}(\varphi_0)\right]^{-1/2}, \end{aligned} \tag{13}$$

and

$$\begin{aligned} \cos\varphi_0' &= -\frac{1+\alpha\xi_\mathrm{CPP}}{\alpha k_\mathrm{H}}b_\mathrm{p}\frac{J_e}{J_\mathrm{p}}\widetilde{U}(\varphi_0'),\\ v_0' &= \frac{\eta\Delta(\varphi_0')\gamma_0 k_\mathrm{H}M_s}{1+\alpha\xi_\mathrm{CPP}}\sin\varphi_0'\cos\varphi_0',\\ \Delta(\varphi_0') &= l_0\left[k_\mathrm{E}+k_\mathrm{H}\sin^2\varphi_0' - \xi_\mathrm{CPP}b_\mathrm{p}\frac{J_e}{J_\mathrm{p}}\widetilde{W}(\varphi_0')\right]^{-\frac{1}{2}}. \end{aligned} \tag{14}$$

For the first branch in Eqs. (13), for the variation $\varphi=\varphi_0+\delta\varphi$, Eq. (11b) provides

$$\frac{\partial(\ln\delta\varphi)}{\partial t} = -\frac{\gamma_0 M_s}{1+\alpha^2}\left\{(-1)^n(1+\alpha\xi_\mathrm{CPP})b_\mathrm{p}\frac{J_e}{J_\mathrm{p}} \times \left(1-c_\mathrm{p}^2\right)^{-1/2}\arccos[(-1)^n c_\mathrm{p}] + \alpha k_\mathrm{H}\right\}. \tag{15}$$

The stability of φ_0—solution requires the terms in curly braces to be positive. This leads to $J_e/J_\mathrm{p} > j_\mathrm{d}$ (n is even) or $J_e/J_\mathrm{p} < j_\mathrm{u}$ (n is odd), where

$$\begin{aligned} j_\mathrm{u} &\equiv \frac{\alpha k_\mathrm{H}}{1+\alpha\xi_\mathrm{CPP}}\frac{\sqrt{1-c_\mathrm{p}^2}}{b_\mathrm{p}\arccos(-c_\mathrm{p})},\\ j_\mathrm{d} &\equiv -\frac{\alpha k_\mathrm{H}}{1+\alpha\xi_\mathrm{CPP}}\frac{\sqrt{1-c_\mathrm{p}^2}}{b_\mathrm{p}\arccos(c_\mathrm{p})}. \end{aligned} \tag{16}$$

For the wall width of this branch, first its existence demands that when n is even (odd), $J_e/J_\mathrm{p} < j_{\Delta\mathrm{u}}$ ($J_e/J_\mathrm{p} > j_{\Delta\mathrm{d}}$) with

$$\begin{aligned} j_{\Delta\mathrm{u}} &\equiv \frac{k_\mathrm{E}}{\xi_\mathrm{CPP}}\frac{2c_\mathrm{p}}{b_\mathrm{p}}\left(\frac{\pi^2}{4}-\arccos^2 c_\mathrm{p}\right)^{-1},\\ j_{\Delta\mathrm{d}} &\equiv -\frac{k_\mathrm{E}}{\xi_\mathrm{CPP}}\frac{2c_\mathrm{p}}{b_\mathrm{p}}\left[\arccos^2(-c_\mathrm{p})-\frac{\pi^2}{4}\right]^{-1}. \end{aligned} \tag{17}$$

Since $\alpha \ll 1$ and $\xi_\mathrm{CPP} \ll 1$, $|j_{\Delta\mathrm{u(d)}}| \gg |j_\mathrm{u(d)}|$ and is usually out of experimental accessibility. Thus, only $j_\mathrm{u(d)}$ is considered when dealing with stability issue. For the variation $\Delta=\Delta(\varphi_0)+\delta\Delta$, Eq. (11c) provides

$$\frac{\pi^2\alpha}{6\gamma_0 M_s}\frac{\partial(\ln\delta\Delta)}{\partial t} = -\frac{2l_0^2}{\Delta^2(\varphi_0)}, \tag{18}$$

implying a stable wall width of this solution branch (see violet solid lines in Fig. 2).

Next we turn to the branch in Eqs. (14). By rewriting the first equation as $J_e/J_\mathrm{p} = -\alpha k_\mathrm{H}\cos\varphi_0'(1-c_\mathrm{p}^2\cos^2\varphi_0')^{1/2}/[(1+\alpha\xi_\mathrm{CPP})b_\mathrm{p}\arccos(c_\mathrm{p}\cos\varphi_0')]$ and analyzing its monotonicity, the permitted current density range of this branch can be obtained. Note that $J_e(\varphi_0') = J_e(2\pi-\varphi_0')$, we then focus on $\varphi_0' \in [0,\pi]$ thus $\sin\varphi_0' \geqslant 0$. After standard calculus, one has

$$\frac{d}{d\varphi_0'}\left(\frac{J_e}{J_\mathrm{p}}\right) = \frac{\alpha k_\mathrm{H}\sin\varphi_0'}{(1+\alpha\xi_\mathrm{CPP})b_\mathrm{p}}\frac{f(\zeta)}{\sqrt{1-\zeta^2}\cdot\arccos^2\zeta}, \tag{19}$$

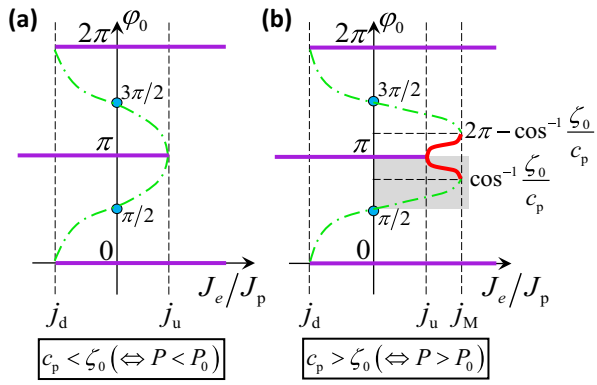

FIG. 2. Illustration of the solution branch in Eqs. (14): (a) $c_p < \zeta_0$, (b) $c_p > \zeta_0$. In both cases, violet solid lines represent the stable solution branch in Eqs. (13) with zero velocity, and green dash-dot curves represent the unstable part of solution branch in Eqs. (14). In addition, red solid curves in (b) indicate the stable part of solution branch in Eqs. (14). The shaded area in (b) will be calculated in details in Fig. 3.

with

$$f(\zeta) = (1-2\zeta^2)\arccos\zeta + \zeta\sqrt{1-\zeta^2}, \quad \zeta \equiv c_p\cos\varphi_0'. \tag{20}$$

On the other hand, the counterpart of Eq. (15) for this solution branch is

$$\frac{\partial(\ln\delta\varphi')}{\partial t} = \frac{\alpha\gamma_0 M_s k_H \sin^2\varphi_0'}{(1+\alpha^2)(1-\zeta^2)\arccos\zeta} f(\zeta), \tag{21}$$

The monotonicity analysis on $f(\zeta)$ provides us a critical value $\zeta_0 = -0.6256$ ($\Leftrightarrow P_0 = 0.3704$) [27]. When $c_p < \zeta_0$ ($\Leftrightarrow P < P_0$), $f(\zeta) > 0$. This fact has two consequences: from Eq. (19), J_e/J_p is an increasing function on $\varphi_0' \in [0, \pi]$ thus acquires its minimum (j_d) at $\varphi_0' = 0$ and maximum (j_u) at $\varphi_0' = \pi$ [see Fig. 2(a)]. However, Eq. (21) tells us that now this whole branch remains unstable and thus is not physically preferred. When $c_p > \zeta_0$ ($\Leftrightarrow P > P_0$), $f(\zeta)$ first increases when φ_0' runs from 0 to $\arccos(\zeta_0/c_p)$ and then decreases when φ_0' exceeds $\arccos(\zeta_0/c_p)$ to π. Correspondingly, J_e/J_p increases from j_d to $j_M = 0.2172\alpha k_H/[(1+\alpha\xi_{CPP})b_p c_p]$ and then decreases to j_u, as illustrated in Fig. 2(b). Meanwhile, from Eq. (21) only when $\arccos(\zeta_0/c_p) < \varphi_0' < 2\pi - \arccos(\zeta_0/c_p)$ the solution branch in Eqs. (14) is stable, which has been marked by red curves in Fig. 2(b).

Now we explain what happens physically when the CPP current density J_e increases from 0 to large positive value. If the wall initially lies in easy xz plane with $\varphi|_{t=0} = 0$, i.e., the magnetization at wall center is parallel to the polarizer, then it always stays in this state with zero velocity no matter how large J_e is. While if the wall initially lies with $\varphi|_{t=0} = \pi$, i.e., the magnetization at wall center is antiparallel to the polarizer, it keeps staying in this state until J_e/J_p increases to j_u. When J_e is further enhanced a little bit, something interesting happens. When the polarizer is not strong enough ($P < P_0$), the wall "jumps" to $\varphi = 0$ state (through $\pi \to 0$ or $\pi \to 2\pi$ route depending on the nature of external disturbances) and then keeps still. On the contrary, if the polarizer is strong enough ($P_0 < P \leqslant 1$), the wall will evolve into one of the two stable parts of the solution branch in Eqs. (14). Likely, which one it runs into is determined by the nature of external disturbances. As J_e/J_p increases from j_u to j_M, the wall acquires a finite velocity as shown by the second equation of Eqs. (14). When J_e/J_p exceeds j_M, the wall jumps to its nearest static branch under external disturbance and then stays in this state.

Next we do some numerical estimations. The following magnetic parameters for Co are adopted (same as those in Ref. [18]): $M_s = 1400$ kA/m, $J = 30 \times 10^{-12}$ J/m, $\alpha = 0.007$ and $\xi_{CPP} = 0.1$. Thus the exchange length $l_0 = 4.94$ nm. The geometry of free layer is $3 \times 50 \times 8000$ nm^3, resulting in three average demagnetization factors: $D_y = 0.917251$, $D_x = 0.082269$ and $D_z = 0.000480$. The crystalline anisotropy and edge roughness are both neglected, thus $k_E = D_x - D_z = 0.081789$ and $k_H = D_y - D_x = 0.834982$. Then $\Delta_0 = l_0/\sqrt{k_E} = 17.3$ nm. As indicated, to obtain stable propagating walls the spin polarization P should satisfy $P > P_0 = 0.3704$. Here we take $P = 0.6$ as an example. Then $b_p = 0.3832$ and $b_p = 0.8442$, thus the extremal point is $\varphi_0^M = \arccos(\zeta_0/c_p) = 0.7657\pi$. The upper limit of the current density for the stable static branch in Eqs. (13) is $J_e^u = j_u \cdot J_p = 7.13 \times 10^6$ A/cm^2. Meanwhile, the upper limit of the current density for the stable finite-velocity branch in Eqs. (14) is $J_e^M = j_M \cdot J_p = 8.82 \times 10^6$ A/cm^2. These two values are both not high for real applications. Then the tilting angle, width, and velocity of a TT ($\eta = -1$) TDW corresponding to the shaded area in Fig. 2(b) are calculated and plotted in Fig. 3. We focus on the red curves, which are the stable part of the finite-velocity branch in Eqs. (14). Interestingly, at $J_e \approx 8.40 \times 10^6$ A/cm^2 the wall can propagate along the LNSV at a velocity as high as 1025 m/s. Therefore planar-transverse polarizers have comparable current efficiency as perpendicular polarizers [18]. To our knowledge, this has never been reported before in existing studies.

Another attracting quantity is the high "differential mobility" (dv/dJ_e) around $J_e = J_e^u$ ($\varphi_0' = \pi$), as shown by the red curve in Fig. 3(c). From Eq. (19), this infinity comes from the divergent behavior of $|d\varphi_0'/dJ_e| \propto 1/|\sin\varphi_0'| \to +\infty$ at $J_e = J_e^u$ ($\varphi_0' = \pi$). Consequently, combining with Eqs. (14), we have $|dv_0'/dJ_e| = |(dv_0'/d\varphi_0') \cdot (d\varphi_0'/dJ_e)| \propto |\cos 2\varphi_0'/\sin\varphi_0'| \to +\infty$. This means that a slight increase of J_e above J_e^u will lead to considerable increase of wall velocity.

To make sure this high differential mobility around $J_e = J_e^u$ is a real effect rather than theoretical illusion, we perform numerical simulations using the OOMMF package [39] with the "Xf_STT" class embedded which enables simulation on injection of multiple spin currents into a ferromagnet in OOMMF. The resulting velocities are depicted by solid squares in Fig. 3(c). The magnetic and geometric parameters are exactly the same with theoretical deductions. In particular, the crystalline anisotropy and edge roughness are both neglected and the demagnetization is turned on. As preparation, a static TDW with $\eta = -1$ and $\phi_0' = \pi$ is generated at the wire center. Perpendicularly injected current density $-J_e\mathbf{e}_y$ manipulates the TDW dynamics. First, a current density pulse with strength 3.0×10^7 A/cm^2 and duration 2.5 ns is applied to slightly push the wall away from its potential valley ($\varphi_0' = \pi$). Then typical current densities ($\leqslant 8.5 \times 10^6$ A/cm^2) are

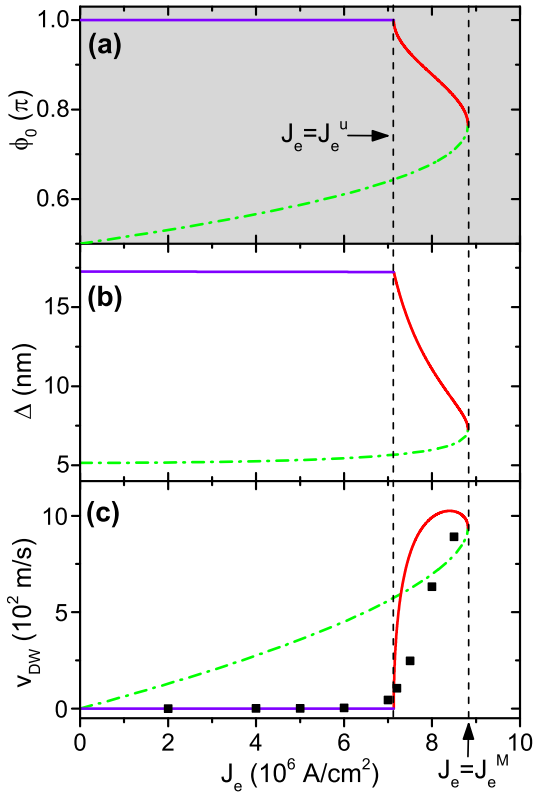

FIG. 3. Dependence of the tilting angle (a), width (b) and velocity (c) of a TDW with $\eta = -1$ on current density in a LNSV with CPP configuration and planar-transverse polarizer ($\mathbf{m}_p = \mathbf{e}_x$). The subfigure (a) corresponds to the shaded area in Fig. 2(b). The free FM layer has the geometry of $50 \times 3 \times 8000$ nm^3, with $M_s = 1400$ kA/m, $J = 30 \times 10^{-12}$ J/m and $\alpha = 0.007$. In addition, $P = 0.6$ and $\xi_{CPP} = 0.1$ for spin-transfer process. The violet solid lines are the stable static branch in Eqs. (13). The red solid (green dash-dot) curves comes from the stable (unstable) part of the finite-velocity branch in Eqs. (14). Solid squares comes from OOMMF simulations.

applied and the wall velocities in stable traveling-wave mode are recorded. Numerical data show that when $J_e < 7.0 \times 10^6$ A/cm^2, the wall creeps forward for a distance and then stops. When $J_e \geqslant 7.0 \times 10^6$ A/cm^2, the wall acquires high velocity very quickly as J_e increases. This critical current density is very close to the theoretical prediction $J_e^u = 7.13 \times 10^6$ A/cm^2. At $J_e = 8.5 \times 10^6$ A/cm^2, the wall velocity is around 900 m/s, which is comparable with the theoretical maximum (1025 m/s at 8.4×10^6 A/cm^2). The difference between theoretical curve and simulation data partially comes from the fact that around J_e^u the half wire with limited length (4 μm) is not enough for the wall to converge to its stable solution Eqs. (14). Another source of deviation comes from the limitation of 1D collective coordinate model in describing real three-dimensional ferromagnets. However, as shown in Fig. 3(c), our 1D analytics does grasp the main results of this issue, that is, high differential mobility around $J_e = J_e^u$ and high wall velocity under low current density ($J_e < 1.0 \times 10^7$ A/cm^2).

In fact, this large differential mobility can be understood physically. By putting Eqs. (5) and (6) into the generalized

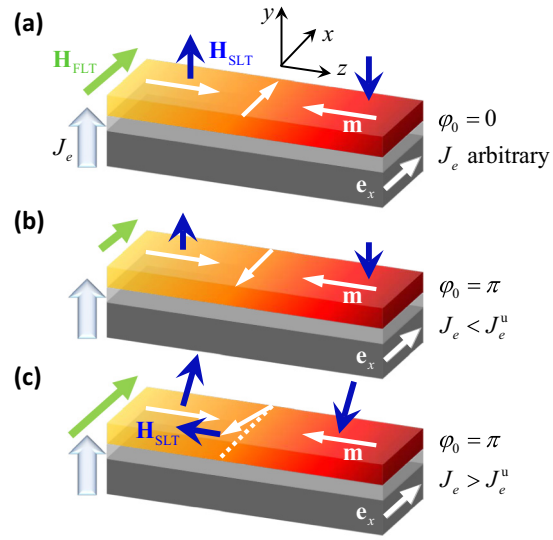

FIG. 4. Illustration of the physical mechanism responsible for the high differential mobility around J_e^u. (a) $\phi_0 = 0$ and J_e is arbitrary. (b) $\phi_0 = \pi$ and $J_e < J_e^u$. (c) $\phi_0 = \pi$ and $J_e > J_e^u$. In all sketches, $\eta = -1$. Green (blue) arrows represent $\mathbf{H}_{FLT}$ ($\mathbf{H}_{SLT}$).

Eular-Lagrangian Eq. (7) with $X = \theta(\phi)$, we obtain the familiar Landau-Lifshitz-Gilbert (LLG) equation,

$$\frac{\partial \mathbf{m}}{\partial t} = -\gamma_0 \mathbf{m} \times \mathbf{H}_{\text{eff}}^0 + \alpha \mathbf{m} \times \frac{\partial \mathbf{m}}{\partial t} - \gamma_0 a_J \mathbf{m} \times (\mathbf{m} \times \mathbf{m}_p) - \gamma_0 b_J \mathbf{m} \times \mathbf{m}_p, \quad (22)$$

where $a_J = \hbar J_e g/(2\mu_0 d e M_s)$, $b_J = \xi_{CPP} a_J$, and $\mathbf{H}_{\text{eff}}^0 = -(\mu_0 M_s)^{-1} \delta \mathcal{E}_0 / \delta \mathbf{m}$. We denote the two effective fields related to SLT and FLT as $\mathbf{H}_{SLT} = a_J(\mathbf{m} \times \mathbf{m}_p)$ and $\mathbf{H}_{FLT} = b_J \mathbf{m}_p$, respectively. Note that Eq. (22) describes a gyrational magnetization dynamics accompanied by a damping-induced motion toward the effective field. For planar-transverse polarizers ($\mathbf{m}_p = \mathbf{e}_x$), $\mathbf{H}_{FLT}$ is always a uniform transverse field directed along $+\mathbf{e}_x$ and thus cannot induce TDW motion along $\mathbf{e}_z$. However, it breaks the twofold symmetry in the x direction: TDWs lying in $\varphi_0 = 0$ plane are always stable while at some critical current density (J_e^u) TDWs initially lying in $\varphi_0 = \pi$ plane will climb out of this potential valley formed by finite hard anisotropy in y direction.

When $J_e < J_e^u$, TDWs are still lying in $\varphi_0 = n\pi$ valleys. Thus, $\mathbf{H}_{SLT}$ is perpendicularly to $\varphi_0 = n\pi$ planes and directed oppositely about the wall center [see Figs. 4(a) and 4(b)]. The gyration around $\mathbf{H}_{SLT}$ leads to temporary wall displacement. At the same time, the damping process results in the tilting of magnetization towards $\mathbf{H}_{SLT}$. Correspondingly, magnetic charges appear at the opposite sides of the free layer and thus generate a magnetostatic field that balances $\mathbf{H}_{SLT}$. As a result, the wall stops and becomes static.

For TDWs initially lying in $\varphi_0 = \pi$ valley and J_e slightly exceeds J_e^u, due to the symmetry about $\varphi_0 = \pi$ plane, the magnetization at wall center departs from it randomly. By denoting the new stable azimuthal angle as φ_0' and from the famous Stoner-Wohlfarth asteroid theorem [40], at critical point one has $H_{FLT} \propto \cos\varphi_0'^3$, which leads to $|d\varphi_0'/dJ_e| \propto |d\varphi_0'/dH_{FLT}| \propto 1/|\sin\varphi_0'| \gg 1$. This explains the high

differential mobility around J_e^{u}. Now we take $0 < \varphi_0' < \pi$ as an example [see Fig. 4(c)], in wall region $\mathbf{H}_{\mathrm{SLT}}$ has $-\mathbf{e}_z$ component. For $\eta = -1$, this leads to a finite velocity along $+\mathbf{e}_z$ which explains the stable branch in Eqs. (14). When current density is too large ($> J_e^{\mathrm{M}}$), the generalized Walker profile will collapse due to the antidirected $\mathbf{H}_{\mathrm{SLT}}$ on the two sides of TDW and vortex/antivortex may emerge, which is out of the scope of this paper.

In summary, dynamical behaviors of TDWs under planar-transverse polarizers in LNSVs with CPP configuration are quite different from known results in two aspects. First, in all well-investigated current-driven stack setups, including FM monolayers (CIP), FM/heavy-metal bilayers (CIP), and LNSVs with parallel and perpendicular polarizers (CPP), TDWs have a finite mobility in the entire range of current density when dealing with a sufficiently smooth and even sample (absence of intrinsic pinning due to imperfectness). This means TDWs will acquire a steady motion with finite velocity under finite charge current density, no matter how small the latter is. However, in LNSVs with strong enough planar-transverse polarizers, steady wall motion with finite velocity can only occur when driving current exceeds a finite threshold of density. Second, at the onset of wall excitation, the differential mobility is very high due to the sudden change in steady tilting angle of TDWs as current density exceeds its lower limit a little bit. This allows TDWs to acquire high velocities under small current densities. The resulting current efficiency is comparable with that of perpendicular polarizers. When the current density exceeds its upper limit, TDWs jump to their nearest static branch. These two exotic behaviors should open possibilities for developing magnetic nanodevices based on TDW propagation with low energy consumption: (a) When polarizers of LNSVs are made of magnetic materials with in-plane rather than perpendicular magnetic anisotropy, high current efficiency is still achievable as long as they are made planar-transverse. (b) The high differential mobility around J_e^{u} makes these LNSVs candidates for high-sensitivity switches, etc.

IV. DW DYNAMICS UNDER PARALLEL AND PERPENDICULAR POLARIZERS

The simulation work by Khvalkovskiy *et al.* proposed the high current efficiency in LNSVs under parallel and perpendicular polarizers with "$\mathbf{m}\cdot\mathbf{m}_{\mathrm{p}}$-independent" STT coefficients [18]. Except for numerics, they also provided a 1D analysis for parallel polarizers in which the wall velocity and tilting angle are two collective coordinates. However, for perpendicular polarizers, the corresponding 1D analysis is absent. Meanwhile, their simulations revealed that under perpendicular (parallel) polarizers, pure SLT (FLT) induces persistent wall displacement while pure FLT (SLT) does not. Therefore, they conjectured that at low currents the large difference for the wall velocities between perpendicular and planar polarizers is related to the factor ξ_{CPP} between the torques. However, the exact ratio of mobilities for these two cases under low currents is not provided. In this section, we perform systematic Lagrangian analysis and provide answers to these issues.

A. Modified Lagrangian and dynamical equations

For $\mathbf{m}\cdot\mathbf{m}_{\mathrm{p}}$-independent STT coefficients, the energy density functional turns to

$$\widetilde{\mathscr{E}}[\mathbf{m}] = \mathscr{E}_0[\mathbf{m}] - \mu_0 M_s \tilde{b}_J p_{\mathbf{m}}, \tag{23}$$

and the dissipation functional becomes

$$\frac{\widetilde{\mathscr{F}}}{\mu_0 M_s^2} = \frac{\alpha}{2}\frac{\dot{\theta}^2 + \dot{\phi}^2\sin^2\theta}{\gamma_0 M_s} - \frac{\tilde{a}_J}{M_s}(p_\theta \sin\theta\dot{\phi} - p_\phi\dot{\theta}), \tag{24}$$

where $\tilde{a}_J = \hbar J_e P/(2\mu_0 deM_s)$ and $\tilde{b}_J = \xi_{\mathrm{CPP}}\tilde{a}_J$. Still, the generalized Walker profile is taken as the configuration space of walls. After putting the wall center position $q(t)$, tilting angle $\varphi(t)$, and width $\Delta(t)$ into Eq. (7) successively, and integrating over $z \in (-\infty, +\infty)$, a new set of dynamical equations are obtained:

$$\alpha\eta\frac{\dot{q}}{\Delta} + \dot{\varphi} = \gamma_0\left(\frac{\pi}{2}\tilde{a}_J p_\varphi + \tilde{b}_J\cos\theta_{\mathrm{p}}\right), \tag{25a}$$

$$\eta\frac{\dot{q}}{\Delta} - \alpha\dot{\varphi} = \gamma_0 M_s k_{\mathrm{H}}\sin\varphi\cos\varphi + \gamma_0\left(\tilde{a}_J\cos\theta_{\mathrm{p}} - \frac{\pi}{2}\tilde{b}_J p_\varphi\right), \tag{25b}$$

$$\frac{\pi^2\alpha}{6}\frac{\dot{\Delta}}{\Delta} = \gamma_0 M_s\left(\frac{l_0^2}{\Delta^2} - k_{\mathrm{E}} - k_{\mathrm{H}}\sin^2\varphi\right) + \gamma_0\pi\tilde{b}_J\sin\theta_{\mathrm{p}}\cos(\varphi - \phi_{\mathrm{p}}). \tag{25c}$$

B. Parallel polarizers

For systematicness, we first briefly revisit TDW dynamics under parallel polarizers. In this case, $\mathbf{m}_{\mathrm{p}} = \mathbf{e}_z$, thus $\theta_{\mathrm{p}} = 0$ and then $p_\varphi = 0$. The dynamical equations turn to

$$\frac{1+\alpha^2}{\gamma_0}\frac{\eta\dot{q}}{\Delta} = \frac{k_{\mathrm{H}}M_s}{2}\sin 2\varphi + (\tilde{a}_J + \alpha\tilde{b}_J), \tag{26a}$$

$$\frac{1+\alpha^2}{\gamma_0}\dot{\varphi} = -\frac{\alpha k_{\mathrm{H}}M_s}{2}\sin 2\varphi + (\tilde{b}_J - \alpha\tilde{a}_J), \tag{26b}$$

$$\frac{\pi^2\alpha}{6\gamma_0 M_s}\frac{\dot{\Delta}}{\Delta} = \frac{l_0^2}{\Delta^2} - k_{\mathrm{E}} - k_{\mathrm{H}}\sin^2\varphi. \tag{26c}$$

The first two equations reproduce Eq. (4) in Khvalkovskiy's work (see Ref. [18]) and the third one provides the TDW width. For the traveling-wave mode of TDW, $\dot{\varphi} = 0$ and $\dot{\Delta} = 0$. This leads to a FLT-determined steady wall velocity:

$$v_0 = \frac{\eta\Delta(\varphi_0)\gamma_0\xi_{\mathrm{CPP}}\tilde{a}_J}{\alpha},$$
$$\sin 2\varphi_0 = \frac{2(\xi_{\mathrm{CPP}} - \alpha)\tilde{a}_J}{\alpha M_s k_{\mathrm{H}}},$$
$$\Delta_1(\varphi_0) = l_0(k_{\mathrm{E}} + k_{\mathrm{H}}\sin^2\varphi_0)^{-1/2}. \tag{27}$$

For variation of φ_0, we have

$$\frac{\partial(\ln\delta\varphi_0)}{\partial t} = -\frac{\alpha\gamma_0 M_s k_{\mathrm{H}}\cos 2\varphi_0}{2(1+\alpha^2)}. \tag{28}$$

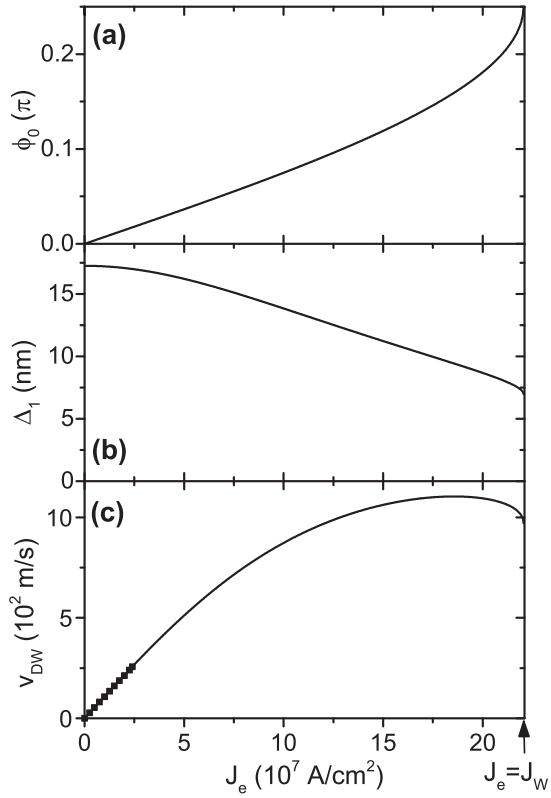

FIG. 5. Dependence of the tilting angle (a), width (b), and velocity (c) of a TDW on current density in a LNSV with CPP configuration and parallel polarizer ($\mathbf{m}_p = \mathbf{e}_z$). The geometry and magnetic parameters of the free layer are the same as those in Fig. 3, except the spin polarization is changed to $P = 0.32$. The solid curves are from Eqs. (27) and the solid squares in (c) are from Fig. 1(b) in Ref. [18] with exactly the same geometric and magnetic parameters.

When $\cos 2\varphi_0 > 0$, i.e., $|\varphi_0 - n\pi| < \pi/4$, the φ_0—solution is stable. On the other hand, for variation of Δ_1, one has

$$\frac{\pi^2\alpha}{6\gamma_0 M_s}\frac{\partial(\delta\Delta)}{\partial t} = -\frac{2l_0^2}{\Delta_1^2(\varphi_0)}\delta\Delta - \Delta_1(\varphi_0)k_H \sin 2\varphi_0 \delta\varphi_0. \tag{29}$$

Thus, the wall width should be stable as long as φ_0 is stable.

Next we compare our analytics with existing simulation data. The geometry and magnetic parameters of the free layer are the same as those in the end of Sec. II, except the spin polarization is changed to $P = 0.32$ (same as in Khvalkovskiy's work). By requiring $|\sin 2\varphi_0| \leqslant 1$, the Walker limit (under which traveling-wave mode survives) is $J_W = \alpha M_s k_H/(2\kappa|\xi_{CPP} - \alpha|) = 2.20 \times 10^8$ A/cm^2. However this is just a theoretical prediction based on the generalized Walker profile. Real simulations (see Fig. 1(b) of Ref. [18]) revealed that TDWs disappear due to global-spin-transfer-induced domain excitation when $J_e > 2.4 \times 10^7$ A/cm^2, which is an order of magnitude smaller J_W. Thus, in traveling-wave mode, at most $\sin^2\varphi_0 \sim 10^{-2}$ and $\Delta_1(\varphi_0) \sim \Delta_0 = 17.3$ nm. This leads to a constant wall mobility $\sim 1.09 \times 10^{-5}$ (m/s)/(A/cm^2), which perfectly explains the linear dependence of wall velocity on current density in Fig. 1(b) of Ref. [18]. In Fig. 5 of our work, analytical results from Eqs. (27) are plotted by solid curves. Meanwhile, numerical data from Fig. 1(b) in Ref. [18] are indicated by solid squares. Obviously, as long as TDWs exist ($J_e < 2.4 \times 10^7$ A/cm^2), our theoretical results are in good agreement with numerical simulations.

C. Perpendicular polarizers

Now $\mathbf{m}_p = \mathbf{e}_y$, thus $\theta_p = \pi/2$ and $\phi_p = \pi/2$. Then $p_\varphi = \cos\varphi$ and Eqs. (25) is simplified to

$$\frac{1+\alpha^2}{\gamma_0}\frac{\eta\dot{q}}{\Delta} = \left[k_H M_s \sin\varphi + \frac{\pi}{2}(\alpha\tilde{a}_J - \tilde{b}_J)\right]\cos\varphi, \tag{30a}$$

$$\frac{1+\alpha^2}{\gamma_0}\dot{\varphi} = \left[\frac{\pi}{2}(\tilde{a}_J + \alpha\tilde{b}_J) - \alpha k_H M_s \sin\varphi\right]\cos\varphi, \tag{30b}$$

$$\frac{\pi^2\alpha}{6\gamma_0 M_s}\frac{\dot{\Delta}}{\Delta} = \left(\frac{l_0^2}{\Delta^2} - k_E - k_H\sin^2\varphi\right) + \frac{\pi\tilde{b}_J}{M_s}\sin\varphi. \tag{30c}$$

For steady traveling-wave mode, we need $\dot{\varphi} = 0$ and $\dot{\Delta} = 0$. This leads to two branches of solution,

$$\varphi_0 = \left(n + \frac{1}{2}\right)\pi, \quad v_0 = 0,$$

$$\Delta_2(\varphi_0) = l_0\left[k_E + k_H - (-1)^n\frac{\pi\tilde{b}_J}{M_s}\right]^{-1/2}, \tag{31}$$

and

$$\sin\varphi_0' = \frac{\pi}{2}\frac{1+\alpha\xi_{CPP}}{\alpha}\frac{\tilde{a}_J}{k_H M_s},$$

$$v_0' = \frac{\pi}{2}\frac{\eta\Delta_2(\varphi_0')\gamma_0\tilde{a}_J}{\alpha}\cos\varphi_0',$$

$$\Delta_2(\varphi_0') = l_0\left(k_E + k_H\sin^2\varphi_0' - \frac{\pi\tilde{b}_J}{M_s}\sin\varphi_0'\right)^{-1/2}. \tag{32}$$

Then we perform stability analysis to these two branches. For the one in Eqs. (31), after taking variation of φ_0 and substituting it into Eq. (30b), one has

$$\frac{\partial(\ln\delta\varphi_0)}{\partial t} = -\frac{\alpha\gamma_0 M_s k_H}{1+\alpha^2}\left[\frac{\pi}{2}\left(\frac{1}{\alpha} + \xi_{CPP}\right)\frac{(-1)^n\tilde{a}_J}{k_H M_s} - 1\right]. \tag{33}$$

Then we define $J_1 \equiv 4|\xi_{CPP} - \alpha|\pi^{-1}(1+\alpha\xi_{CPP})^{-1}J_W$. When $J_e > J_1$ (n is even) or $J_e < -J_1$ (n is odd), $(-1)^n(\alpha^{-1} + \xi_{CPP})\tilde{a}_J\pi/(2k_H M_s) - 1 > 0$ always holds, thus the $\varphi_0 = (n + 1/2)\pi$ solution in the first branch is stable. For the wall width of this branch, similar variational analysis provides the same result as in Eq. (18), implying that the static solution at $\varphi_0 = (n + 1/2)\pi$ always has a stable wall width.

Then we move to the other branch in Eqs. (32). The solution φ_0' requires $|\sin\varphi_0'| \leqslant 1$, which is equivalent to $|J_e| \leqslant J_1$. After varying φ_0' by $\delta\varphi'$ and putting into Eq. (30b), we have

$$\frac{\partial(\ln\delta\varphi')}{\partial t} = -\frac{\alpha\gamma_0 M_s k_H\cos^2\varphi_0'}{1+\alpha^2}, \tag{34}$$

implying that φ_0'—solution is always stable. The corresponding TDW velocity can be explicitly written out as

$$v_0' = \frac{\pi}{2}\frac{\eta\Delta_2(\varphi_0')\gamma_0\tilde{a}_J}{\alpha}(-1)^m\sqrt{1 - \left(\frac{\pi}{2}\frac{1+\alpha\xi_{CPP}}{\alpha k_H M_s}\tilde{a}_J\right)^2}, \tag{35}$$

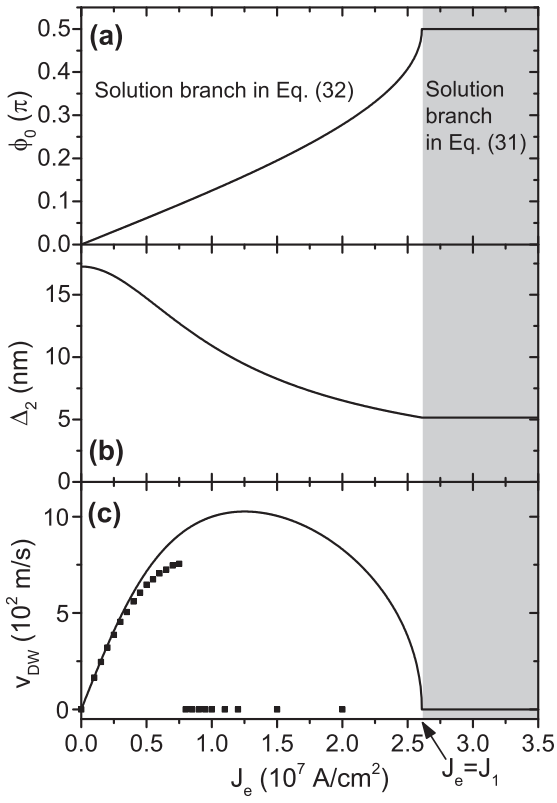

FIG. 6. Dependence of the tilting angle (a), width (b), and velocity (c) of a TDW on current density in a LNSV with CPP configuration and perpendicular polarizer ($\mathbf{m}_p = \mathbf{e}_y$). The geometry and magnetic parameters of the free layer are the same as those in Fig. 5. The solid curves in the white-background area are the solution branch in Eqs. (32) and the solid lines in the shaded area are those from Eqs. (31). The solid squares in (c) are from Fig. 2(b) in Ref. [18].

in which "$(-1)^m$" comes from the initial condition ($\varphi_0'|_{t=0} = m\pi$ at $t = 0$). For $|J_e| \ll J_1$, one has

$$v_0' \approx \frac{\pi}{2}\frac{\eta\Delta_0\gamma_0\tilde{a}_J}{\alpha}(-1)^m. \tag{36}$$

Clearly, it has a mobility larger than that of "parallel-polarizer" case [see Eqs. (27)] by a factor of $\pi/(2\xi_{CPP}) \approx 15.7$, thus well explains the higher current efficiency of perpendicular polarizers. When $|J_e| \to J_1$, the φ_0'—solution converges to φ_0—branch with zero wall velocity.

For the same magnetic parameters as in parallel polarizers, $J_1 = 0.1183J_W = 2.61 \times 10^7$ A/cm^2. For HH TDWs ($\eta = +1$) and standard initial condition ($\varphi_0|_{t=0} = \varphi_0'|_{t=0} = 0$), the solution branch in Eqs. (31) [Eqs. (32)] is plotted in Fig. 6 by solid line (curve) in shaded (white-background) area. In addition, simulation data from Fig. 2(b) in Ref. [18] are depicted in our Fig. 6(c) by solid squares. Clearly, when $J_e \leqslant 0.3 \times 10^7$ A/cm^2, our analytics coincides with simulation data very well. For larger current density, the wall configuration in simulations will be distorted from the standard Walker profile due to global spin transfers, and thus leads to the inconsistency between analytics and simulations.

D. Comparison with experimental data

As mentioned in Sec. I, to our knowledge there are two groups of experimental work. In the first group, currents with definite density inject perpendicularly into LNSVs or half-ring MTJs (genuine CPP configurations). While in the second group, in-plane current flows through zigzag LNSVs and the "vertical spin current" is suggested to be the source of DW velocity boosting; however, the corresponding spin current density is hard to estimate. Therefore, we focus on the first group in which genuine CPP configuration with definite current density is under investigation. Furthermore, our analytics is obtained in a strip geometry (resulting in three averaged demagnetization factors, and hence k_E and k_H), and thus cannot directly apply to half-ring geometry. In summary, the best case to make the comparison is the first case in the first group, which is the experimental work by Boone *et al.* in 2010 [19] on LNSVs with parallel polarizers.

In their work, the free layer is made of the nickel-rich nickel-iron alloy (NRNIA) with $M_s = 430$ kA/m and the crystalline anisotropy is neglected. Its geometry ($3 \times 90 \times 5000$ nm^3) provides three average demagnetization factors: $D_y = 0.9473$, $D_x = 0.05182$ and $D_z = 0.00088$. Thus we have $k_E = D_x - D_z = 0.0509$ and $k_H = D_y - D_x = 0.8955$. The resulting coercive force is $k_E M_s = 275$ Oe, which is consistent with experimental measurements (NRNIA reversal at $+200$ and -300 Oe) in Fig. 2(b) of Ref. [19]. The exchange stiffness (J) has not been explicitly provided. However from the fixed wall width ($\lambda = 53$ nm) they adopted in simulations, we have $J = \mu_0 k_E M_s^2 \lambda^2/2 = 16.6 \times 10^{-12}$ J/m. Furthermore, the conversion coefficient from current density to SLT strength is $\kappa = \tilde{a}_J/J_e = \hbar P/(2\mu_0 deM_s) = 1.32 \times 10^{-3}$ (A/m)/(A/cm^2) for $P = 0.65$. Now we estimate the wall mobility under small driving currents where the wall width can be viewed as constant ($\lambda = 53$ nm). Note that they obtained a damping coefficient from a fitting to the rectified voltage with zero-FLT assumption. However, as indicated by Khvalkovskiy *et al.*, FLT is crucial for TDW dynamics in LNSVs with parallel polarizers. Therefore, we adopt the typical NRNIA value $\alpha = 0.01$ rather than their fitting parameter. Moreover, we assume $\xi_{CPP} = 0.1$, which is the maximum permissible in Ref. [19]. From Eqs. (27), the wall mobility is $|v_0/J_e| = \lambda\gamma_0\xi_{CPP}\kappa/\alpha = 1.55 \times 10^{-4}$ (m/s)/(A/cm^2). This agrees well with their experimental data for $J_e < 2 \times 10^6$ A/cm^2 in their Fig. 4(b). On the other hand, the fitting result $\alpha = 0.09$ leads to a wall mobility of 1.72×10^{-5} (m/s)/(A/cm^2). This is an order of magnitude smaller than the experimental observations and thus should be abandoned.

V. FURTHER BOOSTING BY UTMFS

In real magnetic nondevices composed of LNSVs, to further boost TDW propagation, a UTMF

$$\mathbf{H}_{TMF} = H_\perp(\cos\Phi_\perp, \sin\Phi_\perp, 0) \tag{37}$$

can be applied, with $H_\perp$ and $\Phi_\perp$ being its strength and orientation, respectively. Meanwhile, the pinned layer is assumed to be unaffected, which is a harmless simplification and

will not affect our main conclusion. Nevertheless, rigorous profile and velocity of TDWs under an arbitrary UTMF are hard to obtain due to the mismatch between symmetries in different energy terms in transverse direction. Since we focus on the traveling mode at low current density, the 1D-AEM [28–32] on the LLG equation shall provide useful information. Recalling the results in Sec. III for TDWs moving under planar-transverse polarizers, 1D-AEM is not applicable since stable wall motion with finite velocity can only be excited for current density exceeding a finite threshold. Hence, in this section, we present the results for parallel and perpendicular polarizers.

A. Parallel polarizers

The 1D-AEM needs static profiles of TDWs as the basis to calculate the response of the system under external stimuli. Depending on UTMF strength, static TDWs take different profiles. Therefore, we discuss the "small UTMF" and "finite UTMF" cases separately.

For small UTMFs, the CCP current density, UTMF, and inverse of time are rescaled simultaneously; that is, $\tilde{a}_J = \epsilon\tilde{a}_J^0$, $\tilde{b}_J = \epsilon\tilde{b}_J^0$, $H_\perp = \epsilon h_\perp$ and $1/t = \epsilon(1/\tau)$, where ϵ is the rescaling infinitesimal. The real solution of the LLG equation is expanded as $\Omega(z,t) = \Omega_0(z,\tau) + \epsilon\Omega_1(z,\tau) + O(\epsilon^2)$ with $\Omega = \theta, \phi$. Putting them back into the original LLG Eq. (22), the solution to the zeroth-order equation is the Walker ansatz. At the first order of ϵ, with the help of zeroth-order solutions, the differential equation about θ_1 reads

$$F_s = \mathscr{L}\theta_1, \quad \mathscr{L} \equiv \frac{2J}{\mu_0 M_s}\left(-\frac{d^2}{dz^2} + \frac{\theta_0'''}{\theta_0'}\right),$$
$$F_s \equiv \left[\frac{\eta\alpha(z_0)_\tau}{\gamma_0\Delta_0} - \tilde{b}_J^0\right]\sin\theta_0 + (-1)^n h_\perp \cos\theta_0\cos\Phi_\perp, \tag{38}$$

where $(z_0)_\tau \equiv dz_0/d\tau$ and a prime means d/dz. The subscript s indicates the "small UTMF" case. Note that $\mathscr{L}$ is the same 1D self-adjoint Schrödinger operator as given in Refs. [28–32]. Following the Fredholm alternative, by demanding θ_0' (kernel of $\mathscr{L}$) to be orthogonal to the function F_s defined in Eqs. (38), TDW velocity in traveling-wave mode under small UTMFs is

$$V_s = \varepsilon(z_0)_\tau = \eta\gamma_0\Delta_0\tilde{b}_J/\alpha, \tag{39}$$

which reproduces the rigorous result in Eqs. (27).

For finite UTMFs, we rescale the current density and the TDW velocity (V_f) simultaneously, i.e., $\tilde{a}_J = \varepsilon\tilde{a}_J^0$, $\tilde{b}_J = \varepsilon\tilde{b}_J^0$ and $V_f = \varepsilon v$ in which the subscript f denotes the "finite UTMF" case. By introducing the traveling coordinate $\tilde{z} \equiv z - V_f t = z - \varepsilon v t$, $\theta(z,t)$ and $\phi(z,t)$ are expanded as $\Omega(z,t) = \Omega_0(\tilde{z}) + \varepsilon\Omega_1(\tilde{z}) + O(\varepsilon^2)$ with $\Omega = \theta, \phi$. Substituting them into the LLG equation, an approximate polar angle profile θ_0 (solution to the zeroth-order equations) of the wall is obtained,

$$\ln\frac{\sin\theta_0 - \sin\theta_\infty}{1 + \cos(\theta_0 + \theta_\infty)} = \frac{\eta\tilde{z}}{\Delta(\phi_\infty)/\cos\theta_\infty}, \tag{40}$$

with

$$\phi_\infty = \tan^{-1}\left[k_E \tan\Phi_\perp/(k_E + k_H)\right],$$
$$\theta_\infty = \sin^{-1}\frac{H_\perp}{M_s\sqrt{k_E^2\cos^2\phi_\infty + (k_E + k_H)^2\sin^2\phi_\infty}},$$
$$\Delta(\phi_\infty) = l_0(k_E + k_H\sin^2\phi_\infty)^{-1/2}, \tag{41}$$

in which θ_∞ (ϕ_∞) is the polar (azimuthal) angle of magnetization in domains. At the first order of ϵ, after a similar process as in the field-driven case [30], the equation about θ_1 is

$$\mathscr{L}(\theta_1) = F_f \equiv v\gamma_0^{-1}(\alpha\theta_0' - \sin\theta_0\phi_0') - \tilde{b}_J^0\sin\theta_0, \tag{42}$$

where a "prime" means $d/d\tilde{z}$. Again, θ_0' (kernel of $\mathscr{L}$) should be orthogonal to the function F_f. After similar calculation, TDW velocity in traveling-wave mode under finite UTMF is

$$V_f = u(\theta_\infty)\frac{\eta\gamma_0\Delta(\phi_\infty)\tilde{b}_J}{\alpha},$$
$$u(\theta_\infty) = \frac{2\cos\theta_\infty}{2\cos\theta_\infty - (\pi - 2\theta_\infty)\sin\theta_\infty}. \tag{43}$$

This clearly shows that UTMFs can boost TDW propagation by a factor $u(\theta_\infty)$, which has been well studied in Ref. [30].

B. Perpendicular polarizers

For small UTMFs, after similar rescaling, expansion, and substitution operations, the differential equation about θ_1 is

$$\mathscr{L}\theta_1 = \frac{\eta\alpha(z_0)_\tau\sin\theta_0}{\gamma_0\Delta_0} + (-1)^n\left(h_\perp\cos\theta_0\cos\Phi_\perp - \tilde{a}_J^0\right). \tag{44}$$

The corresponding wall velocity is

$$V_s = \varepsilon(z_0)_\tau = (-1)^n\eta\pi\gamma_0\Delta_0\tilde{a}_J/(2\alpha), \tag{45}$$

which is the $\varphi_0' \to n\pi$ limit of Eqs. (32).

For finite UTMFs, the equation about θ_1 is

$$\mathscr{L}\theta_1 = \frac{v}{\gamma_0}(\alpha\theta_0' - \sin\theta_0\phi_0') - \tilde{a}_J^0\cos\phi_0 + \tilde{b}_J^0\cos\theta_0\sin\phi_0. \tag{46}$$

The existence condition of θ_1—solution provides

$$V_f \approx \omega(\theta_\infty)\frac{\eta\gamma_0\Delta(\phi_\infty)\tilde{a}_J}{\alpha}\cos\phi_\infty,$$
$$\omega(\theta_\infty) = \frac{\pi - 2\theta_\infty}{2\cos\theta_\infty - (\pi - 2\theta_\infty)\sin\theta_\infty}. \tag{47}$$

Simple calculus shows that $\omega(\theta_\infty)$ has a similar divergent behavior as $u(\theta_\infty)$ when $H_\perp \to H_\perp^{\max}$, thus considerably boost TDW motion. Interestingly, in LNSVs with perpendicular polarizers, TDW motion can be manipulated not only by UTMF strength [via $\omega(\theta_\infty)$] but also its orientation (via $\cos\phi_\infty$). This comes from the fact that polarized electrons always act as an extra time-dependent effective field in hard axis. For TDWs with $\phi_\infty \neq n\pi$, magnetization in the wall region rotates around the effective field hence results in a translational wall displacement along $\eta\mathbf{e}_z$ direction. Meanwhile, projection of SLT to the hard axis $\mathbf{e}_y$ contributes to $\cos\phi_\infty$. These lead to the final $\eta\cos\phi_\infty$ factor in Eqs. (47).

VI. SUMMARY

In this paper, TDW dynamics in LNSVs with CPP configurations are systematically investigated within Lagrangian framework. When STT coefficients take Slonczewski's original form, our results show that stable traveling-wave motion of TDWs with finite velocity can survive for strong enough planar-transverse polarizers, with the current efficiency comparable with that of perpendicular ones. More importantly, TDWs have ultrahigh differential mobility around the onset of stable wall excitation. These results should provide insights for developing magnetic nanodevices with low energy consumption. For $\mathbf{m} \cdot \mathbf{m}_p$-independent STT coefficients, analytics for parallel and perpendicular polarizers perfectly explains existing simulations and experiments. Finally, further boosting of TDWs by external UTMFs are investigated with help of 1D-AEM and turns out to be efficient.

ACKNOWLEDGMENTS

M.L. is supported by the Project of Hebei Province Higher Educational Science and Technology Program (QN2019309). Z.A. is funded by the Hebei Province Department of Education (GCC2014025). J.L. acknowledges supports from Natural Science Foundation for Distinguished Young Scholars of Hebei Province of China (A2019205310) and from National Natural Science Foundation of China (Grant No. 11374088).

[1] F. H. De Leeuw, R. Van Den Doel, and U. Enz, Rep. Prog. Phys. **43**, 689 (1980).
[2] Y. Tserkovnyak, A. Brataas, G. E. W. Bauer, and B. I. Halperin, Rev. Mod. Phys. **77**, 1375 (2005).
[3] M. Kläui, J. Phys.: Condens. Matter **20**, 313001 (2008).
[4] D. A. Allwood, G. Xiong, C. C. Faulkner, D. Atkinson, D. Petit, and R. P. Cowburn, Science **309**, 1688 (2005).
[5] M. Hayashi, L. Thomas, R. Moriya, C. Rettner, and S. S. P. Parkin, Science **320**, 209 (2008).
[6] J. H. Franken, H. J. M. Swagten, and B. Koopmans, Nat. Nanotech. **7**, 499 (2012).
[7] J. Münchenberger, G. Reiss, and A. Thomas, J. Appl. Phys. **111**, 07D303 (2012).
[8] S. S. P. Parkin and S.-H. Yang, Nat. Nanotech. **10**, 195 (2015).
[9] M. Li, J. Wang, and J. Lu, New J. Phys. **21**, 053011 (2019).
[10] J. Slonczewski, J. Magn. Magn. Mater. **159**, L1 (1996).
[11] Z. Li and S. Zhang, Phys. Rev. Lett. **92**, 207203 (2004).
[12] G. Tatara, H. Kohno, and J. Shibata, Phys. Rep. **468**, 213 (2008).
[13] J. Grollier, D. Lacour, V. Cros, A. Hamzic, A. Vaurès, and A. Fert, D. Adam, and G. Faini, J. Appl. Phys. **92**, 4825 (2002).
[14] J. Grollier, P. Boulenc, V. Cros, A. Hamzić, A. Vaurès, A. Fert, and G. Faini, Appl. Phys. Lett. **83**, 509 (2003).
[15] C. K. Lim, T. Devolder, C. Chappert, J. Grollier, V. Cros, A. Vaurès, A. Fert, and G. Faini, Appl. Phys. Lett. **84**, 2820 (2004).
[16] A. Rebei and O. Mryasov, Phys. Rev. B **74**, 014412 (2006).
[17] K. Kawabata, M. Tanizawa, K. Ishikawa, Y. Inoue, M. Inuishi, and T. Nishimura, in *2011 International Conference on Simulation of Semiconductor Processes and Devices, 8-10 September 2011, Osaka, Japan* (IEEE, Piscataway, NJ, 2011), pp. 55–58.
[18] A. V. Khvalkovskiy, K. A. Zvezdin, Ya. V. Gorbunov, V. Cros, J. Grollier, A. Fert, and A. K. Zvezdin, Phys. Rev. Lett. **102**, 067206 (2009).
[19] C. T. Boone, J. A. Katine, M. Carey, J. R. Childress, X. Cheng, and I. N. Krivorotov, Phys. Rev. Lett. **104**, 097203 (2010).
[20] A. Chanthbouala, R. Matsumoto, J. Grollier, V. Cros, A. Anane, A. Fert, A. V. Khvalkovskiy, K. A. Zvezdin, K. Nishimura, Y. Nagamine, H. Maehara, K. Tsunekawa, A. Fukushima, and S. Yuasa, Nat. Phys. **7**, 626 (2011).
[21] P. J. Metaxas, J. Sampaio, A. Chanthbouala, R. Matsumoto, A. Anane, A. Fert, K. A. Zvezdin, K. Yakushiji, H. Kubota, A. Fukushima, S. Yuasa, K. Nishimura, Y. Nagamine, H. Maehara, K. Tsunekawa, V. Cros, and J. Grollier, Sci. Rep. **3**, 1829 (2013).
[22] J. Sampaio, S. Lequeux, P. J. Metaxas, A. Chanthbouala, R. Matsumoto, K. Yakushiji, H. Kubota, A. Fukushima, S. Yuasa, K. Nishimura, Y. Nagamine, H. Maehara, K. Tsunekawa, V. Cros, and J. Grollier, Appl. Phys. Lett. **103**, 242415 (2013).
[23] S. Pizzini, V. Uhlíř, J. Vogel, N. Rougemaille, S. Laribi, V. Cros, E. Jiménez, J. Camarero, C. Tieg, and E. Bonet, Appl. Phys. Express **2**, 023003 (2009).
[24] V. Uhlíř, S. Pizzini, N. Rougemaille, J. Novotny, V. Cros, E. Jiménez, G. Faini, L. Heyne, F. Sirotti, C. Tieg, A. Bendounan, F. Maccherozzi, R. Belkhou, J. Grollier, A. Anane, and J. Vogel, Phys. Rev. B **81**, 224418 (2010).
[25] V. Uhlíř, S. Pizzini, N. Rougemaille, V. Cros, E. Jiménez, L. Ranno, O. Fruchart, M. Urbánek, G. Gaudin, J. Camarero, C. Tieg, F. Sirotti, E. Wagner, and J. Vogel, Phys. Rev. B **83**, 020406(R) (2011).
[26] V. Uhlíř, J. Vogel, N. Rougemaille, O. Fruchart, Z. Ishaque, V. Cros, J. Camarero, J. C. Cezar, F. Sirotti, and S. Pizzini, J. Phys.: Condens. Matter **24**, 024213 (2012).
[27] P.-B. He, Eur. Phys. J. B **86**, 412 (2013).
[28] A. Goussev, R. G. Lund, J. M. Robbins, V. Slastikov, and C. Sonnenberg, Phys. Rev. B **88**, 024425 (2013).
[29] A. Goussev, R. G. Lund, J. M. Robbins, V. Slastikov, and C. Sonnenberg, Proc. R. Soc. A **469**, 20130308 (2013).
[30] J. Lu, Phys. Rev. B **93**, 224406 (2016).
[31] M. Li, J. B. Wang, and J. Lu, Sci. Rep. **7**, 43065 (2017).
[32] M. Yu, M. Li, and J. Lu, Nanomaterials **9**, 128 (2019).
[33] R. D. McMichael and M. J. Donahue, IEEE Trans. Magn. **33**, 4167 (1997).
[34] Y. Nakatani, A. Thiaville, and J. Miltat, J. Magn. Magn. Mater. **290**, 750 (2005).
[35] N. Rougemaille, V. Uhlíř, O. Fruchart, S. Pizzini, J. Vogel, and J. C. Toussaint, Appl. Phys. Lett. **100**, 172404 (2012).
[36] N. L. Schryer and L. R. Walker, J. Appl. Phys. **45**, 5406 (1974).
[37] C. T. Boone and I. N. Krivorotov, Phys. Rev. Lett. **104**, 167205 (2010).
[38] J. Shibata, G. Tatara, and H. Kohno, J. Phys. D **44**, 384004 (2011).
[39] M. J. Donahue and D. G. Porter, OOMMF User's Guide, Version 1.0, Interagency Report NISTIR 6376 (National Institute of Standards and Technology, Gaithersburg, MD, Sept 1999), http://math.nist.gov/oommf.
[40] C. Tannous and J. Gieraltowski, Eur. J. Phys. **29**, 475 (2008).